

# Intricacies and Mechanism of *p*-Doping Spiro-MeOTAD Using Cu(TFSI)<sub>2</sub>

Adrian Hochgesang, Simon Biberger, Jeannine Grüne, John Mohanraj, Frank-Julian Kahle, Vladimir Dyakonov, Anna Köhler, and Mukundan Thelakkat\*

Copper salts are a popular choice as *p*-dopants for organic semiconductors, particularly in N<sup>2</sup>,N<sup>2</sup>,N<sup>2</sup>,N<sup>2</sup>,N<sup>7</sup>,N<sup>7</sup>,N<sup>7</sup>,N<sup>7</sup>-octakis(4-methoxyphenyl)-9,9'-spirobi[9H-fluoren]-2,2',7,7'-tetramine (Spiro-MeOTAD) hole transport material for solar cells. While being exceptionally effective, no scientific consensus about their doping mechanism has been established so far. This study describes the thermodynamic equilibria of involved species in copper(II) bis(trifluoromethanesulfonyl)imide (Cu(TFSI)<sub>2</sub>) doped, co-evaporated Spiro-MeOTAD. A temperature-independent formation of charge transfer states is found, followed by an endothermic release of free charge carriers. Impedance and electron paramagnetic resonance spectroscopy unravel low activation energies for hole release and hopping transport. As a result, (52.0 ± 6.4)% of the total Cu(TFSI)<sub>2</sub> molecules form free, dissociated holes at 10 mol% and room temperature. Cu<sup>I</sup> species arising out of doping are stabilized by formation of a [Cu<sup>I</sup>(TFSI)<sub>2</sub>]<sup>-</sup> cuprate, inhibiting elemental copper formation. This Cu<sup>I</sup> species presents a potent hole trap reducing their mobility, which can be averted by simple addition of a bathocuproine complexing agent. A nonlinear temperature-dependent conductivity and mobility that contradicts current charge transport models is observed. This is attributed to a combination of trap- and charge transfer state freeze-out. These insights may be adapted to other metal salts, providing guidelines for designing next-generation ultra-high efficiency dopants.

of interfaces, extracting photogenerated charge carriers fast, efficient and selective is crucial for high-performance solar cells.<sup>[1]</sup> N<sup>2</sup>,N<sup>2</sup>,N<sup>2</sup>,N<sup>2</sup>,N<sup>7</sup>,N<sup>7</sup>,N<sup>7</sup>,N<sup>7</sup>-octakis(4-methoxyphenyl)-9,9'-spirobi[9H-fluoren]-2,2',7,7'-tetramine (Spiro-MeOTAD) has found widespread use as a hole transport material (HTM) in solar cell research, where it is commonly *p*-doped (i.e., oxidizing Spiro-MeOTAD) by air (O<sub>2</sub>) with the help of LiTFSI additives to increase the free charge carrier density.<sup>[2,3]</sup> Li et al. first incorporated copper(I) thiocyanate and copper(I) iodide into Spiro-MeOTAD HTM and found distinct benefits such as improved power conversion efficiency and HTM conductivity over conventional dopants like LiTFSI/O<sub>2</sub> or the cobalt complex FK209.<sup>[4]</sup> This concept was refined by other groups designing stable copper(II) complexes with tunable valance band levels and solubilities by counter-ion choice.<sup>[5-7]</sup> We replaced the solution doping using copper salts by a solvent free and highly controlled co-evaporation route employing copper(II) bis(trifluoromethanesulfonyl)imide Cu(TFSI)<sub>2</sub> as a *p*-type dopant to yield con-

ductive, uniform, and pinhole-free HTM layers. Our concept was previously successfully applied to conventional MAPbI<sub>3</sub> based 3D perovskite solar cells.<sup>[8]</sup> While practically proven to be useful in perovskite solar cells, the field still lacks a conclusive picture of the physical and chemical processes inside the Cu<sup>II</sup> doped Spiro-MeOTAD bulk. Especially the role of dopant side

## 1. Introduction

Ever since the advent of organic solar cells and recent, but fast improvements in perovskite solar cells, a profound understanding of the fine interplay in these multilayer devices becomes a focus of research. With an ever-growing number

A. Hochgesang, J. Mohanraj, M. Thelakkat  
Applied Functional Polymers  
University of Bayreuth  
95440 Bayreuth, Germany  
E-mail: mukundan.thelakkat@uni-bayreuth.de

S. Biberger, F.-J. Kahle, A. Köhler  
Soft Matter Optoelectronics  
Department of Physics  
University of Bayreuth  
95440 Bayreuth Germany

J. Grüne, V. Dyakonov  
Experimental Physics VI  
Faculty of Physics and Astronomy  
University of Würzburg  
97074 Würzburg, Germany

A. Köhler, M. Thelakkat  
Bavarian Polymer Institute (BPI) and Bayreuth Institute of Macromolecular Research (BIMF)  
University of Bayreuth  
95440 Bayreuth, Germany

 The ORCID identification number(s) for the author(s) of this article can be found under <https://doi.org/10.1002/aelm.202200113>.

© 2022 The Authors. Advanced Electronic Materials published by Wiley-VCH GmbH. This is an open access article under the terms of the Creative Commons Attribution License, which permits use, distribution and reproduction in any medium, provided the original work is properly cited.

DOI: 10.1002/aelm.202200113

products on charge transport is unclear, which turns out to be of quite complex nature. To close this gap, we herein report the occurring thermodynamic equilibria between redox states in co-evaporated, Cu(TFSI)<sub>2</sub> doped Spiro-MeOTAD necessary to draw a complete picture of the doping process and discuss the consequences thereof. First, the theoretically predicted and experimentally observed doping reaction of Cu(TFSI)<sub>2</sub> with Spiro-MeOTAD was investigated using ultraviolet photoelectron- and UV/vis/NIR absorption spectroscopy. Temperature controlled optical spectroscopy experiments are used to gain insight into the formation of charge transfer (CT) states as the product of the doping reaction. Via electron paramagnetic resonance spectroscopy (EPR), electrical conductivity and impedance spectroscopy, possible endothermic release of free charge carriers by dissociation of the CT state was monitored. We quantitatively pin-point the activation energies for CT dissociation  $E_{A,CT}$  by temperature dependent studies.

A low  $E_{A,CT}$  may result in high doping efficiencies even at increased dopant loadings, which will be experimentally verified in the course of this work. The mobility and thermodynamic equilibria of the bound and unbound charge carriers are investigated in detail by impedance- and EPR spectroscopy. Further, we determine the influence of the thermodynamic equilibria on the thermal activation energy for fundamental hopping processes  $E_{A,Hop}$ . Well-documented electronic properties of pristine Spiro-MeOTAD such as

temperature-dependent mobility are thoroughly compared to that of Cu(TFSI)<sub>2</sub> doped samples. Distinct nonlinearities in conductivity, carrier concentration and mobility for Cu(TFSU)<sub>2</sub> doped Spiro-MeOTAD below 150 K are extensively studied. We try to shed light on the source of non-linear behavior by investigating reversible CT- and trap state recombination with the help of [Cu(MeCN)<sub>4</sub>]BF<sub>4</sub> as a model Cu<sup>I</sup> source. Additional focus is set on the influence of dopant products on charge transport in the bulk.

## 2. Results and Discussion

### 2.1. Charge Transfer Formation

We investigate the doping mechanism of Cu-salts in Spiro-MeOTAD by first considering the process of charge transfer formation in thin films. In a typical *p*-doping experiment, the dopant is required to possess unoccupied energy levels deeper in energy than the highest occupied molecular orbital (HOMO) of the organic semiconductor (OSC).<sup>19,10</sup> If this condition is met, an exothermic electron transfer from OSC to dopant can be expected. By using UV photoelectron spectroscopy (UPS) we measured the ionization potential (IP), which is by Koopmans-theorem in first approximation identical to the HOMO, and workfunction of Spiro-MeOTAD (Figure 1a).<sup>11</sup> The electron

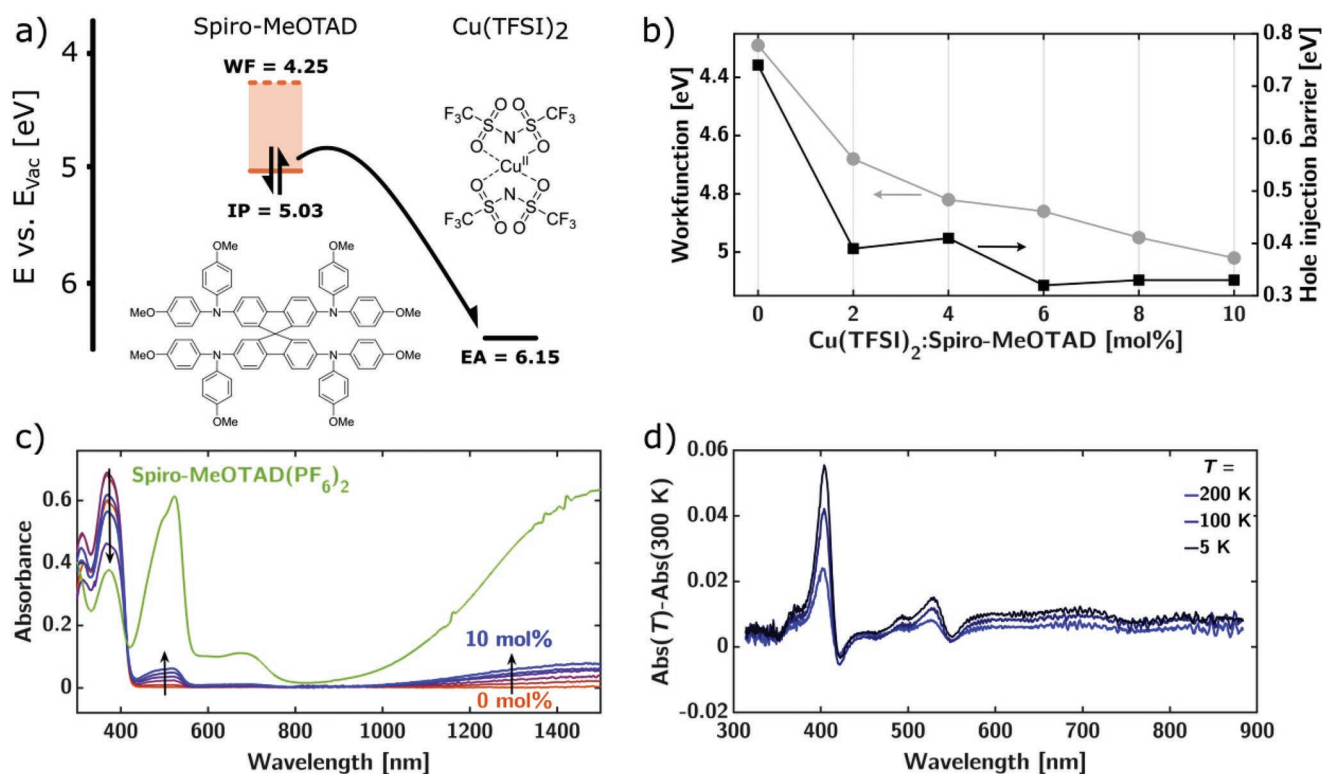


**Figure 1.** a) Energy level diagram of pristine Spiro-MeOTAD (orange) and Cu(TFSI)<sub>2</sub> (black) as determined by UPS (WF and IP of Spiro-MeOTAD) and CV (EA of Cu(TFSI)<sub>2</sub>). b) Workfunction (left, grey circles) and hole-injection barrier HIB (right, black squares) of co-evaporated Spiro-MeOTAD films with increasing Cu(TFSI)<sub>2</sub> molar ratio. c) UV/vis/NIR absorption spectra of co-evaporated films with increasing molar ratios of Cu(TFSI)<sub>2</sub> highlighting the formation of spectral features identical to that of chemically synthesized, pure Spiro-MeOTAD(PF<sub>6</sub>)<sub>2</sub> (green). d) Difference in optical absorption of 10 mol% Cu(TFSI)<sub>2</sub> doped Spiro-MeOTAD thin film UV/vis spectra obtained at 200 K (blue), 100 K (dark blue), and 5 K (black) to the spectrum obtained at 300 K (see Figure S3, Supporting Information).

affinity EA with respect to vacuum level of  $\text{Cu}(\text{TFSI})_2$  was calculated from CV half-wave reduction potentials according to a known literature procedure (Figure S1, Supporting Information).<sup>[12]</sup> An electron affinity of EA = 6.15 eV of  $\text{Cu}(\text{TFSI})_2$  and IP = 5.03 eV of pristine Spiro-MeOTAD w.r.t. vacuum level were determined. Clearly, the EA of  $\text{Cu}(\text{TFSI})_2$  is positioned 1.12 eV deeper than the Spiro-MeOTAD HOMO, facilitating electron transfer. The removal of electrons from Spiro-MeOTAD upon doping is expected to result in a downshift of the workfunction toward the HOMO of the OSC. We monitored this electron transfer by UPS in a second experiment on co-evaporated Spiro-MeOTAD thin films with 0–10 mol%  $\text{Cu}(\text{TFSI})_2$  dopant ratio (Figure 1b). A continuous decrease of the workfunction from 4.25 eV down to 5.02 eV was recorded. This downshift was verified by a decreasing hole-injection barrier HIB (the difference between HOMO and workfunction) shown in Figure 1b. We noticed a slight variation in HOMO position during doping, which is responsible for the unexpectedly pronounced decrease of HIB between 2 and 4 mol% (See also summary of all UPS values collected in Table S1, Supporting Information). From Figure 1b, two distinct processes can be discerned: first, a strong initial HIB drop of  $\approx 740$  meV in the pristine state to 390 meV at 2 mol%  $\text{Cu}(\text{TFSI})_2$ . This steep HIB gradient marks the region, where  $E_F$  moves through a lower density of states per energy interval compared to the deeper lying valence band. We assign these states lying higher in energy as trap states, that is, the generated holes are being consumed entirely in passivating these trap states above the valence band up to 2 mol%  $\text{Cu}(\text{TFSI})_2$ .<sup>[13]</sup> We clearly differentiate those trap states from trap states originating from dopant products, which are characterized in Section 2.4. Despite the high purity of Spiro-MeOTAD used in this work of 99.9% (HPLC, see Supporting Information for manufacturer details), reducing impurities are common for organic semiconductors, shifting the Spiro-MeOTAD intrinsic carrier density from  $\approx 9 \times 10^{14} \text{ cm}^{-3}$  published by Abate et al. to  $1.2 \times 10^{17} \text{ cm}^{-3}$  in this work (see Section 2.1).<sup>[14]</sup> However, we propose the influence of these intrinsic trap states on subsequent doping experiments to be low, being fully passivated after 2 mol%  $\text{Cu}(\text{TFSI})_2$  (Figure 1b). Further, the characteristic slope change of  $E_F$  (dopant concentration) has also been associated with the Fermi level crossing an mid-gap acceptor level, which originates from dopant:host interaction.<sup>[15]</sup> Second, for doping concentrations greater than 2 mol%, the Fermi level  $E_F$  (e.g., workfunction) is pinned at  $\approx 330$  meV above the Spiro-MeOTAD valence band. At this stage it can be assumed, that the dopant releases free holes, which moves  $E_F$  closer to the HOMO with a shallow slope.<sup>[16–18]</sup> Fortifying the designated role as a hole conductor, the workfunction of 5.02 eV at 10 mol%  $\text{Cu}(\text{TFSI})_2$  allows for a very efficient injection of holes in the co-evaporated Spiro-MeOTAD films using high workfunction electrodes such as Au. Due to the twisted nature of the spiro-core inducing steric hindrance and bulky (nonplanar) form of the Spiro-MeOTAD, we expect Spiro-MeOTAD and  $\text{Cu}(\text{TFSI})_2$  to react according to an integer charge transfer. This infers that no hybridization of frontier orbitals (HOMO or lowest unoccupied molecular orbital) takes place and the system can be treated like a conventional redox-couple forming CT states upon doping.<sup>[19]</sup> Optical UV/vis/NIR absorption spectroscopy was employed as a powerful tool to study the CT state evolution in 0–10 mol%

$\text{Cu}(\text{TFSI})_2$  doped Spiro-MeOTAD thin films (Figure 1c; Figure S2, Supporting Information). Simultaneous vacuum co-evaporation was used to deposit high-quality, pinhole-free thin films on glass, circumventing solvent influence and miscibility issues (see Supporting Information for experimental details).<sup>[8]</sup>

The ground-state absorption of Spiro-MeOTAD at 370 nm is continuously bleached upon adding  $\text{Cu}(\text{TFSI})_2$ , with new peaks emerging at 517 nm, 687 nm, and 1445 nm (see Figure S2, Supporting Information, for difference spectrum). The broad NIR absorption at 1445 nm was assigned to intervalence charge-transfer (IV-CT) from a positively charged radical-cation triphenylamine to the linking biphenyl bridge.<sup>[20]</sup> In addition, a characteristic fingerprint for charged Spiro-MeOTAD species is the absorption at 517 nm (as well as 687 nm).<sup>[21]</sup> We conclude a steady formation of charged Spiro-MeOTAD species upon co-evaporation with  $\text{Cu}(\text{TFSI})_2$ , complementing earlier studies by Mohanraj et al.<sup>[8]</sup> To study the thermodynamic nature of the CT state formation, we carried out temperature dependent absorption spectroscopy on co-evaporated films (Figure 1d, see Supporting Information, for spectra of all doping concentrations). No significant change in absorption intensity of the 517 nm band is observable. As a consequence, we conclude the formation of the CT states to be temperature independent, in line with experiments by Tietze et al. on doped small molecules.<sup>[22]</sup> Lastly, we want to shed light on the nature of the charged Spiro-MeOTAD species. Three stable oxidation states of Spiro-MeOTAD are known in literature, namely Spiro-MeOTAD<sup>1+</sup>, Spiro-MeOTAD<sup>2+</sup>, and Spiro-MeOTAD<sup>4+</sup>.<sup>[23]</sup> UPS studies on Spiro-MeOTAD(PF<sub>6</sub>)<sub>4</sub> revealed a HOMO energy of 5.25 eV, which is situated 0.90 eV above the EA of  $\text{Cu}(\text{TFSI})_2$ . Consequently, all oxidation products of Spiro-MeOTAD are theoretically accessible by exothermic electron transfer to  $\text{Cu}(\text{TFSI})_2$ , showcasing its capabilities as a powerful *p*-type dopant. For experimental identification of the formed oxidation state, we synthesized chemically pure Spiro-MeOTAD<sup>2+</sup> by reacting Spiro-MeOTAD with two equivalents of the single-electron oxidant NOPF<sub>6</sub>. Thin films of the obtained Spiro-MeOTAD(PF<sub>6</sub>)<sub>2</sub> were characterized by UV/vis/NIR spectroscopy (Figure 1c, green curve). We noted very similar optical absorption features between pure Spiro-MeOTAD(PF<sub>6</sub>)<sub>2</sub> and the  $\text{Cu}(\text{TFSI})_2$  doped Spiro-MeOTAD. However, we cannot reliably distinguish the two oxidation states Spiro-MeOTAD<sup>1+/2+</sup> due to i) both states being almost degenerate in energy, with a separation of less than 110 mV versus Ag/Ag<sup>+</sup> resp. Fc/Fc<sup>+</sup> and ii) a very similar optical absorption spectral profile.<sup>[21,24]</sup> A comparison with Spiro-MeOTAD(PF<sub>6</sub>)<sub>4</sub> absorption spectrum reveals, that Spiro-MeOTAD(PF<sub>6</sub>)<sub>4</sub> is characterized by a broad peak at 875 nm, which is absent in our experiments (Figure 1c).<sup>[23]</sup> Therefore, both Spiro-MeOTAD<sup>1+</sup> and Spiro-MeOTAD<sup>2+</sup> are presumed as the most probable products of Spiro-MeOTAD doped with  $\leq 10$  mol% Cu (TFSI).

After proving the temperature-independent formation of charged Spiro-MeOTAD<sup>1+/2+</sup> CT states upon doping by optical absorption spectroscopy and UPS, the next step is to investigate the dissociation of the CT state and generation of mobile charge carriers. However, the CT state, being a salt, can be subject to strong coulombic binding energies in the range of  $>100$  meV.<sup>[22]</sup> Thus, a certain activation energy must be provided in order to separate CT states into free carriers. Only free charge carriers

can contribute to the observed macroscopic conductivity in disordered organic semiconductors by thermally activated hopping processes. Our group has monitored and reported the change in electrical conductivity by measuring current-voltage scans of Spiro-MeOTAD:Cu(TFSI)<sub>2</sub> co-evaporated on top of interdigitated Au electrodes in a previous study.<sup>[8]</sup>

Upon co-evaporating Cu(TFSI)<sub>2</sub>, a linear increase followed by conductivity saturation (at 6 mol% Cu(TFSI)<sub>2</sub>) with an average value of  $\approx 7 \times 10^{-4} \text{ S cm}^{-1}$  was observed, in agreement with the constant HIB found in our UPS experiments above 6 mol% dopant. Elevated temperatures in the Spiro-MeOTAD effusion cell during evaporation do not significantly enhance the charge carrier density, as evidenced by the low conductivity ( $1 \times 10^{-7} \text{ S cm}^{-1}$ ) of the evaporated pristine Spiro-MeOTAD sample. Increase in electrical conductivity values demonstrate the presence of mobile charge carriers in Spiro-MeOTAD:Cu(TFSI)<sub>2</sub> co-evaporated samples.

Here, we intend to quantify this observation by determining the amount of free charge carriers  $p$  in the doped bulk via solid state Mott-Schottky experiments. More precisely, this analysis yields the density of ionized acceptors (from dopants)  $N_A^-$  in the bulk, which is equal to the density of free holes  $p$  in the hole conductor, since charge neutrality must be obeyed. This is achieved by measuring the voltage dependent capacitance  $C(V)$  of a metal-insulator-semiconductor device stack such as FTO/Al<sub>2</sub>O<sub>3</sub>/Hexamethyldisilazane/Cu(TFSI)<sub>2</sub>:Spiro-MeOTAD/

Au using impedance spectroscopy. Since the spatial width of a depletion layer (which in turn dictates its electrical capacitance) is very sensitive to the number of free carriers present in the semiconductor, measuring the series capacitance can give information about  $N_A^-$ . Applying a negative bias voltage causes the formation of a charge carrier depletion zone at the insulator/ $p$ -type semiconductor interface, which changes the overall device capacitance. By evaluating the slope  $dC^{-2}/dV$  of the device capacitance versus applied potential, the number of free carriers  $N_A^-$  can be evaluated (Figure 2a, see Figure S4, Supporting Information, for exemplary fit). In agreement with a very strong decrease in HIB and increase in conductivity when adding 2 mol% Cu(TFSI)<sub>2</sub>, the charge carrier density rises from  $1.2 \times 10^{17} \text{ cm}^{-3}$  to  $1.0 \times 10^{19} \text{ cm}^{-3}$  at 1.5 mol% dopant. Above 1.5 mol%,  $N_A^-$  is increasing in a linear fashion up to  $3.2 \times 10^{19} \text{ cm}^{-3}$  at 10 mol% without showing saturation effects (Figure 2b). Having successfully quantified the density of free carriers, we focus on the density of bound CT states. Contrary to Mott-Schottky analysis, which is sensitive to only free charge carriers in the bulk, EPR detects all paramagnetic species within the sample volume. Specifically, EPR is used to determine the absolute sum of bound (in the form of a CT state) and free charge carriers. For measuring EPR, we co-evaporated Cu(TFSI)<sub>2</sub> and Spiro-MeOTAD onto poly(ethylene terephthalate) substrates of known area with a defined thickness, which were consequently sealed in quartz

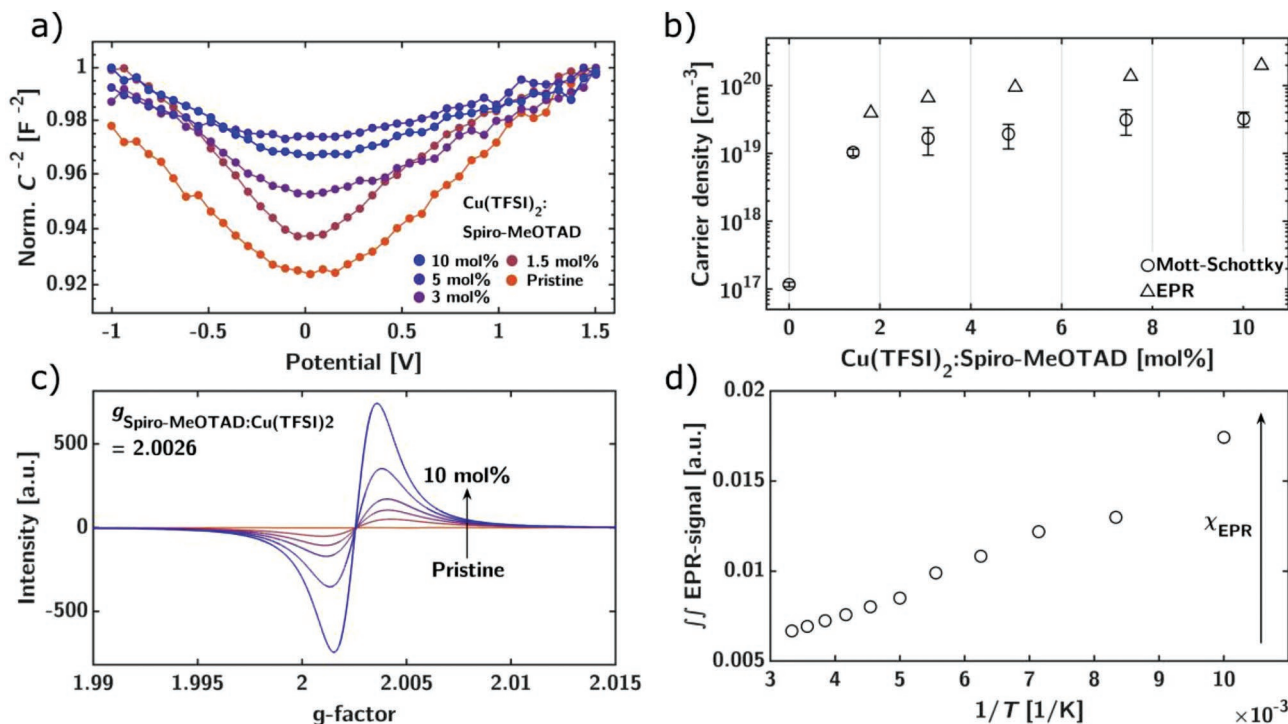


**Figure 2.** a) Exemplary, normalized  $C^{-2}$  versus applied potential plot of metal-insulator-semiconductor (MIS) devices fabricated with an FTO/Al<sub>2</sub>O<sub>3</sub>/Hexamethyldisilazane/Cu(TFSI)<sub>2</sub> doped Spiro-MeOTAD/Au structure. Negative potentials deplete the majority charge carriers (holes) from the interface, decreasing the capacitance. The positive slope in the positive potential range indicates low frequency inversion at the insulator/Spiro-MeOTAD interface. b) Charge carrier/spin densities obtained by Mott-Schottky (circles) and EPR (triangles) measurements. c) Doping concentration dependent EPR spectra of Cu(TFSI)<sub>2</sub> doped Spiro-MeOTAD thin films, co-evaporated on PET substrates. Modulation amplitude  $B_{\text{mod}} = 0.02 \text{ mT}$ , microwave power  $P_{\text{MW}} = 0.8 \text{ mW}$ . d) Double integral (proportional to spin susceptibility, i.e., spin density) of the EPR signal as a function of the inverse temperature proves localized spin species (Curie contribution). Doping concentration = 7.5 mol%.

tubes under inert atmosphere. The EPR parameters are optimized for the highest signal of the 10 mol% doped film ( $B_{\text{mod}} = 0.02$  mT,  $P_{\text{MW}} = 0.8$  mW). As a fact, the presence of paramagnetic  $\text{Cu}^{\text{II}}$  ions is not affecting the results, as they cannot be resolved with the optimized parameters (Figure S5, Supporting Information).  $\text{Cu}^{\text{I}}$  cations are diamagnetic due to a  $4s^0 3d^{10}$  electron configuration and therefore EPR inactive.<sup>[25]</sup> With increasing dopant concentration, the Lorentzian shaped EPR peak increases in area (Figure 2c). A  $g$ -value of 2.0026 was found, comparable to H-TFSI and Li-TFSI/ $\text{O}_2$  doped Spiro-MeOTAD.<sup>[26–28]</sup> By convention, the EPR spectra (Figure 2c) are displayed as the first derivative of the original microwave absorption signal, thus double integration yields the absolute number of paramagnetic species  $N_{\text{Spins}}$ , normalized to unit volume and referenced to a sample with known spin concentration (Figure 2b). The quantity  $N_{\text{Spins}}$  includes all paramagnetic species per unit volume, whether bound to a counter ion (CT state) or free to move under the influence of an electric field (free holes  $p$ ).  $N_{\text{Spins}}$  follows the same doping concentration dependent trend as  $N_{\text{A}^-}$ , yet we noticed a constant offset, which is equal to the states not detectable by Mott–Schottky measurements, the bound CT states. They contribute to about a factor of 4–6 in the range of 3–10 mol% doping ratio. It should be emphasized, that no information about the ratio between free and in CT states bound carriers can be deduced from the absolute number of spins  $N_{\text{Spins}}$ , owing to their high absolute error. Depending on the spin reference used, the absolute error is up to 1 order of magnitude, yet their relative values used in this work are exact. Hence, we used impedance spectroscopy to determine the ratio between bound and free charge carriers (see Section 2.3). Aiming to understand the evolution of ratio between  $N_{\text{A}^-}$  and  $N_{\text{Spins}}$  upon doping, we correlated both values with the UV/vis/NIR CT state absorbance integral from our previous experiment (Figure 1c). Both  $N_{\text{A}^-}$  and  $N_{\text{Spins}}$  were found to increase monotonically and linearly with the absorbance integral (Figure S6, Supporting Information). This indicates, that no additional EPR silent species or bipolaron species are formed at up to 10 mol%  $\text{Cu}(\text{TFSI})_2$ . Notably, the electrical conductivity saturates despite a monotonical increase in  $N_{\text{A}^-}$  and  $N_{\text{Spins}}$ , which hints to effects of the doping on the carrier mobility  $\mu$  and will be discussed in the next paragraph in detail.

Finally, for charge transport considerations later in this work, it is necessary to understand the degree of charge carrier localization in  $\text{Cu}(\text{TFSI})_2$  doped Spiro-MeOTAD. For this, we conducted temperature dependent EPR measurements on one typical sample (7.5 mol%  $\text{Cu}(\text{TFSI})_2$  doped Spiro-MeOTAD). The double integral of the EPR signal is proportional to the susceptibility  $X$  and was found to depend linearly on the inverse sample temperature  $1/T$  in our experiment (Figure 2d).<sup>[29,30]</sup> It is well described by Curie contribution ( $\approx N_{\text{Spins}}/T$ ), characteristic for localized spin species. The linear trend underlines the absence of additional paramagnetic species arising at different temperatures, which would induce a deviation from  $1/T$  behavior, fitting to temperature-independent formation of CT states.<sup>[30]</sup> By correcting the internal spin reference density to the cavity temperature, we verified a temperature-independent spin density  $N_{\text{Spins}}(T)$  for a 7.5 mol%  $\text{Cu}(\text{TFSI})_2$  doped sample (Figure S7, Supporting Information).

When extrapolating to the  $y$ -axis intercept, an offset remains in the magnitude of the determination inaccuracy. Nevertheless, Pauli contribution, that is, band like transport, is not typical for Spiro-MeOTAD even at high concentrations, as discussed below. Hence, free charge carriers are formed at room temperature in  $\text{Cu}(\text{TFSI})_2$  doped Spiro-MeOTAD, increasing the macroscopic bulk conductivity via hopping in mostly localized sites. To conclude, the ratio between free and in CT states bound charge carriers was determined and their changes upon varying the dopant concentration.

## 2.2. Charge Transport

As we quantified the nature and density of reaction products formed in  $\text{Cu}(\text{TFSI})_2$  doped Spiro-MeOTAD, we proceed further to complete the microscopic description of charge transport and thermally activated processes leading to free charge carriers. To select a proper model capable of describing the charge transport, we recorded the temperature dependent conductivity  $\sigma(T)$  of co-evaporated  $\text{Cu}(\text{TFSI})_2$  doped Spiro-MeOTAD thin films from 400 K to 20 K in a He-cryostat (Figure 3a).

Focusing on the pristine sample, a distinct linear region was found between 400 K and 150 K. We observed a positive slope  $d\sigma/dT$ , clearly indicating a temperature activated hopping behavior. Commonly, the popular Mott law is employed to model  $\sigma(T)$  in organic semiconductors.<sup>[31]</sup> As it assumes a constant density of states surrounding the Fermi energy, which can hardly be assumed, we refer to Efros-Shklovskii variable range hopping (ES-VRH) accounting for a Coulomb gap surrounding  $E_{\text{F}}$ .<sup>[32,33]</sup> As Spiro-MeOTAD is disordered in terms of the energetic landscape with localized, spatially randomly distributed states (amorphous nature), the ES-VRH model is sufficient to explain the pristine case.<sup>[33]</sup> In addition, this model accounts for a Coulomb interaction of localized states introduced by the dopant molecules and hopping distances exceeding the nearest neighbor distance at low temperatures.<sup>[34,35]</sup> ES-VRH predicts the dependence  $\ln(\sigma/\sigma_0) \propto T^{-1/2}$  and the experimental data on pristine Spiro-MeOTAD is in accordance to this.<sup>[34,36]</sup> In  $\text{Cu}(\text{TFSI})_2$  doped Spiro-MeOTAD samples, we noticed a restriction of the linear  $\sigma(T)$  region to smaller temperature ranges (Figure 3a). Additionally, in all doped samples, a distinct temperature independent behavior is found below 150 K. Li et al. pointed out, that a temperature independent charge carrier transport in organic semiconductors may be explained sufficiently within the VRH model framework. At high carrier densities and low temperatures, Li proposed that the energy required for a carrier hop is provided entirely by the electric field across the device. This implies, that no thermal activation is necessary and the transport can be described as field-assisted tunnelling in the low temperature regime.<sup>[37]</sup> We could qualitatively adapt Lis modified VRH model to  $\sigma(T)$  of  $\text{Cu}(\text{TFSI})_2$  doped Spiro-MeOTAD using  $N_{\text{A}^-}$  from Mott–Schottky measurements (Figure 2b; Figure S13, Supporting Information). Applying Lis theory, one could assume the origin of  $\sigma(T)$  nonlinearities in  $\text{Cu}(\text{TFSI})_2$  doped Spiro-MeOTAD to stem from field-assisted tunnelling. Yet, carefully analyzing Lis model suggests a similar trend for the temperature dependent mobility  $\mu(T)$  if the Fermi level  $E_{\text{F}}$

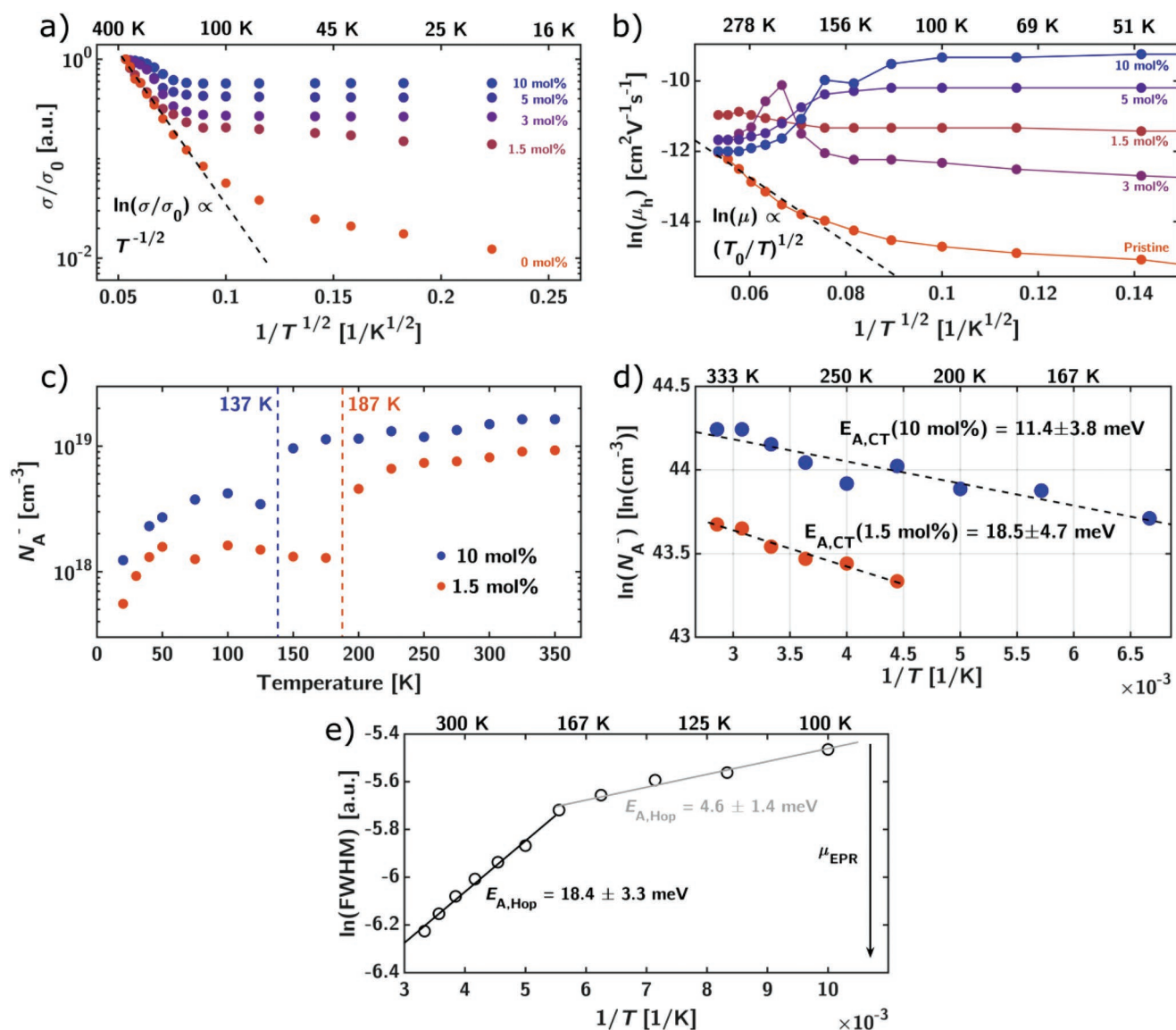


**Figure 3.** a) Temperature dependent, individually normalized conductivities  $\sigma$  measured on FTO/Cu(TFSI)<sub>2</sub>:Spiro-MeOTAD/Au devices with different doping concentrations from 400 K to 20 K. b) Temperature dependent hole mobilities  $\mu_h$  of Cu(TFSI)<sub>2</sub> doped Spiro-MeOTAD, determined from impedance measurements on FTO/Cu(TFSI)<sub>2</sub>:Spiro-MeOTAD/Au devices using the negative differential susceptance  $-\Delta B$ . Black dashed fit line shows typical ES-VRH behavior  $\ln(\mu_h) \propto (T_0/T)^{1/2}$  in the case of pristine Spiro-MeOTAD sample. All values were obtained at a constant electrical field  $F = 100 \text{ kV cm}^{-1}$ . Full temperature scale measurements are shown in Figure S10, Supporting Information, detailed temperature dependent  $-\Delta B$  versus frequency spectra in Figure S11, Supporting Information. c) Temperature dependent charge carrier densities  $N_A^-(T)$  of 1.5 mol% and 10 mol% Cu(TFSI)<sub>2</sub> doped Spiro-MeOTAD, determined by Mott-Schottky measurements. A vertical dotted line demarcates the freeze-out points, for example, the thermal energy available below these marked values is not sufficient to dissociate the intimate CT pair. d) Arrhenius-type temperature dependency of  $N_A^-(T)$  measured via Mott-Schottky experiments above the freeze-out point (150 K for 10 mol% Cu(TFSI)<sub>2</sub> (blue), resp. 200 K for 1.5 mol% (orange)) with fitted activation energies  $E_{A,CT}$ . e) Logarithmic EPR linewidth (FWHM) of a 7.5 mol% Cu(TFSI)<sub>2</sub> doped Spiro-MeOTAD thin film as a function of inverse temperature. An activation energy for hole transport  $E_{A,Hop} = (18.4 \pm 3.3) \text{ meV}$  (black fit) for higher temperature and  $(4.6 \pm 1.4) \text{ meV}$  (grey fit) below 160 K can be determined. Full temperature dependent EPR spectra can be found in Figure S12, Supporting Information.

and  $N_A^-$  are considered constant; i.e., a monotonic mobility decrease followed by a weakly temperature dependent region at lower temperatures. As a consequence, temperature dependent conductivity measurements are not sufficient to analyze the origin of nonlinear  $\sigma(T)$ , which shifts our focus toward temperature dependence of charge carrier mobility  $\mu$ .

To probe the temperature dependent mobility of free charge carriers in Cu(TFSI)<sub>2</sub> doped Spiro-MeOTAD, we carried out

impedance spectroscopy experiments on FTO/Cu(TFSI)<sub>2</sub>:Spiro-MeOTAD/Au metal-semiconductor devices employing the negative differential susceptance method (see Supporting Information for details). Using a metal-semiconductor device structure, holes are injected at one electrode if a sufficient electrical field  $F$  across the device is applied. By measuring the capacitive response of the biased device at different frequencies, an average carrier transit time for a given organic layer

thickness and electrical field can be deduced, even at moderate bulk conductivities of doped semiconductor samples (where most common methods fail). Indium-tin-oxide/Li(TFSI) doped Spiro-MeOTAD/Au devices have recently been used to study the Spiro-MeOTAD charge carrier mobility via negative differential susceptance by Li et al. Carrier densities of up to  $2.8 \times 10^{19} \text{ cm}^{-3}$  were reported using Mott–Schottky measurements, proving the applicability of this method for highly doped Spiro-MeOTAD samples.<sup>[38]</sup> Again, pristine Spiro-MeOTAD follows a temperature activated behavior, characterized by an increase in carrier mobility upon heating the sample up to 400 K. Between 350 K and 175 K,  $\ln(\mu)$  is proportional to the inverse sample temperature. Closer analysis yields a slope of 0.5, thus resembling

ES-VRH dependency for the hole mobility with  $\ln(\mu) \propto \left(\frac{T_0}{T}\right)^{1/2}$ , where  $T_0 = 8.5 \times 10^3 \text{ K}$ . (Figure 3b).<sup>[39]</sup> We like to point out, that for the temperature range between 350 K to 20 K, a poor fit was found for  $\ln(\mu) \propto \left(\frac{1}{T}\right)^2$  predicted by models using a Gaussian

density of states distribution, which are often employed in literature to describe the electrical behaviour of doped organic semiconductors (Figure S14, Supporting Information).<sup>[40]</sup> Röhr et al. obtained comparable  $\mu(T)$  of undoped Spiro-MeOTAD in space charge limited current device data fitted by Mott–Gurney law, verifying the negative differential susceptance method used in this experiment.<sup>[41]</sup> Consequently,  $\sigma(T)$  and  $\mu(T)$  of pristine Spiro-MeOTAD is described sufficiently by the ES-VRH model. To our surprise, doped samples are clearly subject to a different nature of charge transport, even increasing in charge carrier mobility upon cooling the sample below a threshold point of  $\approx 150 \text{ K}$ , followed by a temperature independent region between 150 K and 20 K (Figure 3b). We further note, that the negative correlation  $d\mu/dT < 0$  is exclusive to higher doping concentrations  $\geq 5 \text{ mol\%}$ . At this point we want to highlight, that a negative temperature coefficient mobility is no unambiguous fingerprint of band-like transport typically found in metals. Exemplary, similar behavior was found in poly(2,5-bis(3-tetra-decylthiophen-2-yl)thieno[3,2-b]thiophene) PBTBT field-effect transistors, explained by Luttinger liquid behavior.<sup>[42]</sup> Additionally, Spiro-MeOTAD, even at high doping ratios, cannot be described in terms of band transport due to the large amount of energetic disorder.<sup>[43]</sup> Thus, invoking VRH models, which expect a monotonic decrease in mobility and conductivity, are not able to explain the nonlinear charge transport in Cu(TFSI)<sub>2</sub> doped Spiro-MeOTAD samples.

Based on the relationship  $\sigma = qN_A^- \mu$  with  $q$  being the elementary charge, we formulate the lack of thermal energy at low temperatures to dissociate the CT-state as a possible cause for the nonlinearities found in Cu(TFSI)<sub>2</sub> doped Spiro-MeOTAD. Intuitively, this so-called carrier freeze-out would be reflected in  $N_A^-(T)$ , necessitating a quantification. For this, we coupled the Mott-Schottky experimental setup as described in an earlier paragraph with a Helium cryostat. Figure 3c shows  $N_A^-(T)$  measurements on 1.5 and 10 mol% Cu(TFSI)<sub>2</sub> doped Spiro-MeOTAD between 20 K and 350 K. Here we observe a sharp jump in carrier density at 137 K (for 10 mol% dopant) and 187 K (1.5 mol% dopant), which we denote as transition points. Above these transition points,  $N_A^-$  is proportional to the sample

temperature. At lower temperatures, we noticed a decrease in free carrier concentration for both samples. Ultimately,  $N_A^-$  is not correlated to the sample temperature below these transition temperatures. We assign the distinct loss in free carrier concentration  $N_A^-$  at low temperatures to the recombination of free holes and counterion to re-form the bound CT state (freeze-out). Above the freeze-out,  $N_A^-(T)$  can be well described by a Arrhenius type activation process, with the activation energy  $E_{A,CT}$  corresponding to the CT state dissociation energy (Figure 3d).<sup>[22]</sup>  $E_{A,CT}$  decreases from  $(18.5 \pm 4.7) \text{ meV}$  at 1.5 mol% Cu(TFSI)<sub>2</sub> to  $(11.4 \pm 3.8) \text{ meV}$  at 10 mol%, presumably due to increased energetic disorder, facilitating CT state dissociation.<sup>[22]</sup> These values are directly reflected in the freeze-out temperatures of 187 K and 137 K, which translate to thermal energy values of 16.1 meV (1.5 mol%) and 11.8 meV (10 mol%).  $E_{A,CT}$  is in line with previously published results of disordered systems, ranging from 9 to 54 meV.<sup>[22]</sup> The measured freeze-out temperatures yield first evidence for our hypothesis, overlapping with the mid-point temperatures of nonlinear effects of  $\sigma(T)$  and  $\mu(T)$  (Figure 3a,b).

We aim to fortify our hypothesis by approaching the thermodynamics of carrier hopping. Our previous  $\mu(T)$  measurements (Figure 3b) clearly show an increase in carrier mobility below the freeze-out. Therefore, we test the correlation between the average activation energy  $E_{A,Hop}$  for carrier site transition (a “hop”) and  $N_A^-(T)$ . The full width at half maximum (FWHM) of an EPR signal can be related to the average microscopic charge carrier mobility  $\mu_{EPR}$  in doped organic systems.<sup>[30]</sup> In general, increasing microscopic mobility narrows the EPR linewidth due to averaging of hyperfine interactions (motional narrowing).<sup>[28,44]</sup> Subsequently, we determined  $E_{A,Hop}$  by evaluating the FWHM of the EPR signal of a 7.5 mol% doped sample for different temperatures and applying Arrhenius fits (Figure 3e). With increasing temperature, the FWHM decreases continuously, indicating increasing mobility in doped samples. A distinct change in slope occurred for  $\text{FWHM}_{EPR}(T)$  at  $\approx 180 \text{ K}$ , with a greater slope  $d(\ln(\text{FWHM}_{EPR}))/d(1/T)$  above 180 K. The more decreasing EPR linewidth above 180 K is in contrast to impedance measurements (Figure 3b), where we observed a decrease in mobility upon increasing temperature between 150 K and 400 K for doped Spiro-MeOTAD. This can be explained by the fact that the linewidth of EPR is only affected by mobile polarons that arise after dissociation of CT states in this experiment (no active electron/hole injection via electrodes). In contrast, any trap states created simultaneously reduce the overall mobility of impedance spectroscopy by trapping the injected holes. We recorded an  $E_{A,Hop}$  of  $(18.4 \pm 3.3) \text{ meV}$  above 180 K, with  $(4.6 \pm 1.4) \text{ meV}$  below for Arrhenius fits on  $\text{FWHM}_{EPR}(T)$  (Figure 3e). The transition temperature of 180 K ( $\approx 16 \text{ meV}$  thermal energy) fits to the CT state dissociation energies  $E_{A,CT} = 11.4\text{--}18.5 \text{ meV}$  for 1.5 and 10 mol% Cu(TFSI)<sub>2</sub> doped Spiro-MeOTAD (Figure 3c). From  $\text{FWHM}_{EPR}(T)$  and  $N_A^-(T)$  experiments we conclude, that the CT state freeze-out is directly influencing the carrier mobility and it is consequently responsible for the nonlinear conductivity of Cu(TFSI)<sub>2</sub> doped Spiro-MeOTAD. Both  $E_{A,Hop}$  and  $E_{A,CT}$  can be verified by linking them to the macroscopic observed thermal activation energy for conductivity  $E_{A,\sigma}$ . We analyzed  $E_{A,\sigma}$  by Arrhenius fits on temperature dependent conductivity measurements of

co-evaporated  $\text{Cu}(\text{TFSI})_2$  doped Spiro-MeOTAD films (Figure S15, Supporting Information). Privitera et al. pointed out, that  $E_{A,\sigma}$  is the sum of both CT state binding energy  $E_{A,CT}$  and hole transport activation energy  $E_{A,Hop}$ .<sup>[30]</sup> As displayed in Figure S16, Supporting Information,  $E_{A,\sigma}$  values ranging from  $(39.0 \pm 7.0)$  meV to  $(130.0 \pm 15.9)$  meV were recorded for the  $\text{Cu}(\text{TFSI})_2$  doped Spiro-MeOTAD system, with most samples having values below 100 meV.  $E_{A,\sigma}$  of  $\text{F}_4\text{TCNQ}$  doped Spiro-MeOTAD was reported as ca. 170 meV, generally the thermal activation energies for conductivity are broadly distributed for small molecule organic semiconductors, ranging roughly from 38 to 467 meV.<sup>[45,46]</sup> In comparison,  $\text{Cu}(\text{TFSI})_2$  doped Spiro-MeOTAD displays rather small  $E_{A,\sigma}$  values. This result is remarkably well in line with an expected, approximated value of  $E_{A,CT}(10 \text{ mol}\%) + E_{A,Hop}(7.5 \text{ mol}\%) \approx 30$  meV. Higher measured  $E_{A,\sigma}$  values are likely the result of additional factors such as electrostatic disorder of CT states (Figure S16, Supporting Information).<sup>[46]</sup> Summarizing, we were able to resolve all three major activation energy contributions to the doping process  $E_{A,\sigma}$  (for conductivity),  $E_{A,CT}$  (release of free charge carriers) and  $E_{A,Hop}$  (hopping of free charge carriers). We conclude the nonlinear conductivity and mobility of  $\text{Cu}(\text{TFSI})_2$  doped Spiro-MeOTAD to be caused by reversible CT state freeze out.

### 2.3. Doping Efficiency

As discussed earlier, we found  $E_{A,CT}$  of  $\text{Cu}(\text{TFSI})_2$  doped Spiro-MeOTAD to be low compared to other doped organic semiconductors, for example, in the case of  $N,N,N',N'$ -tetrakis(4-methoxyphenyl)benzidine (4-MeO-TPD) doped with  $\text{C}_{60}\text{F}_{36}$ ,  $\approx 30$  meV are required for CT state dissociation.<sup>[17]</sup> To test, if a low  $E_{A,CT}$  facilitates carrier release in doped organic systems, we investigated the doping efficiency  $\eta_{\text{Dop}}$ . This figure of merit quantifies the ratio between free, dissociated charge carriers  $p$  and total density of dopant molecules in the system  $N_A$  as  $\eta_{\text{Dop}} = p/N_A$ .  $N_A^-$  was determined by Mott-Schottky experiments described in Section 2.1, where we assumed that the number of free holes  $p$  equals  $N_A^-$ . It is worth emphasizing, that the neutrality condition  $p = N_A^-$  may not hold true for very high trap densities or a large number of free carriers bound in the CT state.<sup>[17,22]</sup> A detailed derivation of  $N_A$  can be found in the Supporting Information. Defining  $\eta_{\text{Dop}}$  via  $N_{\text{Spins}}$  and  $N_A^-$  was omitted due to the introduction of a large error source in absolute number of spins. As shown in Figure 4a, co-evaporated  $\text{Cu}(\text{TFSI})_2$  doped Spiro-MeOTAD retains a doping efficiency of up to  $(52.0 \pm 6.4)$  % at 10 mol% dopant. Thus, in general  $\eta_{\text{Dop}}$  improves dramatically compared to other popular  $p$ -dopants, which drop below the 10.3% mark

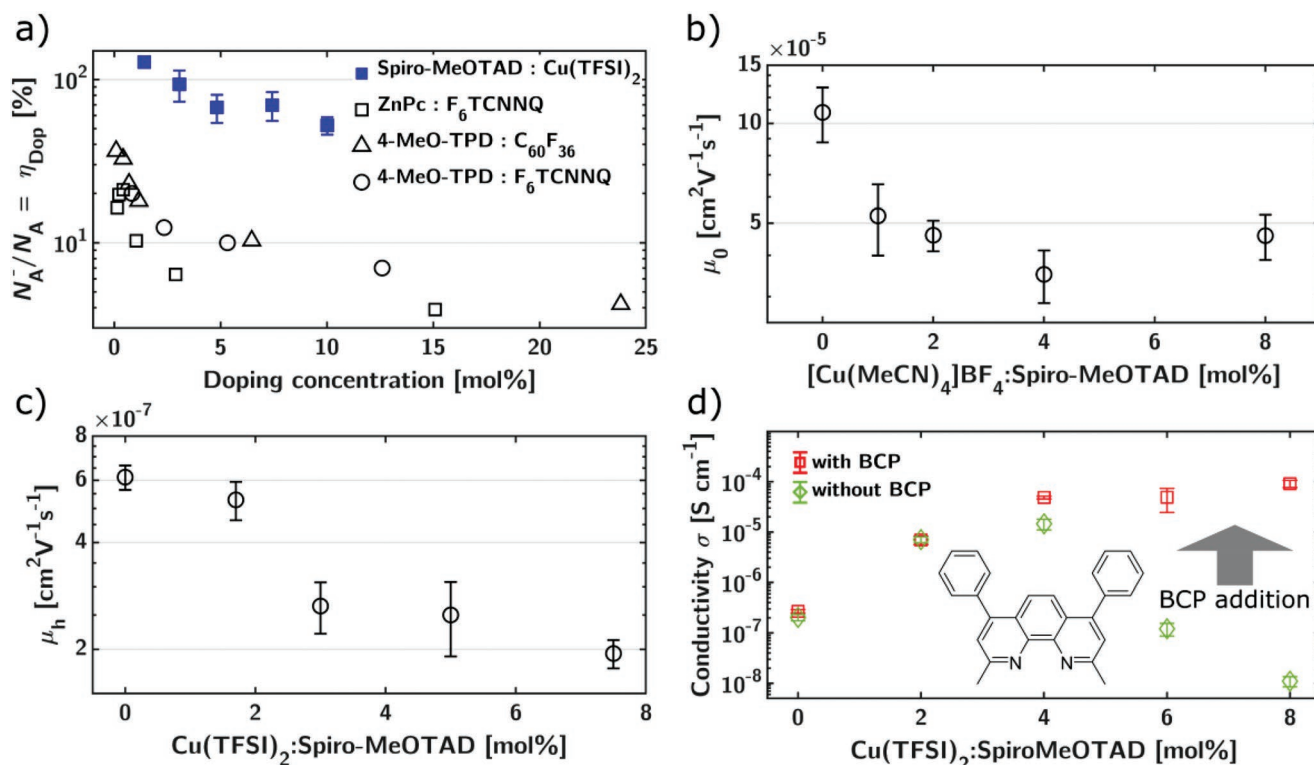


**Figure 4.** a) Doping efficiencies for different doping concentrations of  $\text{Cu}(\text{TFSI})_2$ :Spiro-MeOTAD (blue squares). See Supporting Information for detailed information. Literature values for small molecule semiconductors: Zink-Phthalocyanine (abbr. ZnPc) doped with  $\text{F}_6\text{TCNNQ}$  (squares), 4-MeO-TPD doped with  $\text{C}_{60}\text{F}_{36}$  (triangles) and  $\text{F}_6\text{TCNNQ}$  (circles).<sup>[17,22]</sup> b) Zero-field mobilities  $\mu_0$  of solution processed Spiro-MeOTAD thin films mixed with different molar amounts of  $[\text{Cu}(\text{MeCN})_4]\text{BF}_4$ . c) Mobility  $\mu$  of co-evaporated thin films of  $\text{Cu}(\text{TFSI})_2$  doped Spiro-MeOTAD using the CELIV method on FTO/ $\text{Al}_2\text{O}_3$ / $\text{Cu}(\text{TFSI})_2$ :Spiro-MeOTAD/Au devices. d) Thin film conductivities of solution processed,  $\text{Cu}(\text{TFSI})_2$  doped Spiro-MeOTAD without (green diamonds) and with bathocuproine (BCP, structure shown in graph) additive (red squares) at different dopant concentrations. BCP was added in equimolar amounts to  $\text{Cu}(\text{TFSI})_2$ .

at only 6.4 mol% in the case of the most efficient system in this series, C<sub>60</sub>F<sub>36</sub> doped 4-MeO-TPD. Typically,  $\eta_{\text{Dop}}$  strongly decreases with increasing doping concentration, because charge carrier capture processes by dopant molecules become more likely.<sup>[17]</sup> In summary, the extraordinary low CT state binding energy  $E_{\text{A,CT}}$  found in the Spiro-MeOTAD:Cu(TFSI)<sub>2</sub> system helps to greatly boost the doping efficiency compared to previously published *p*-dopants for organic systems.

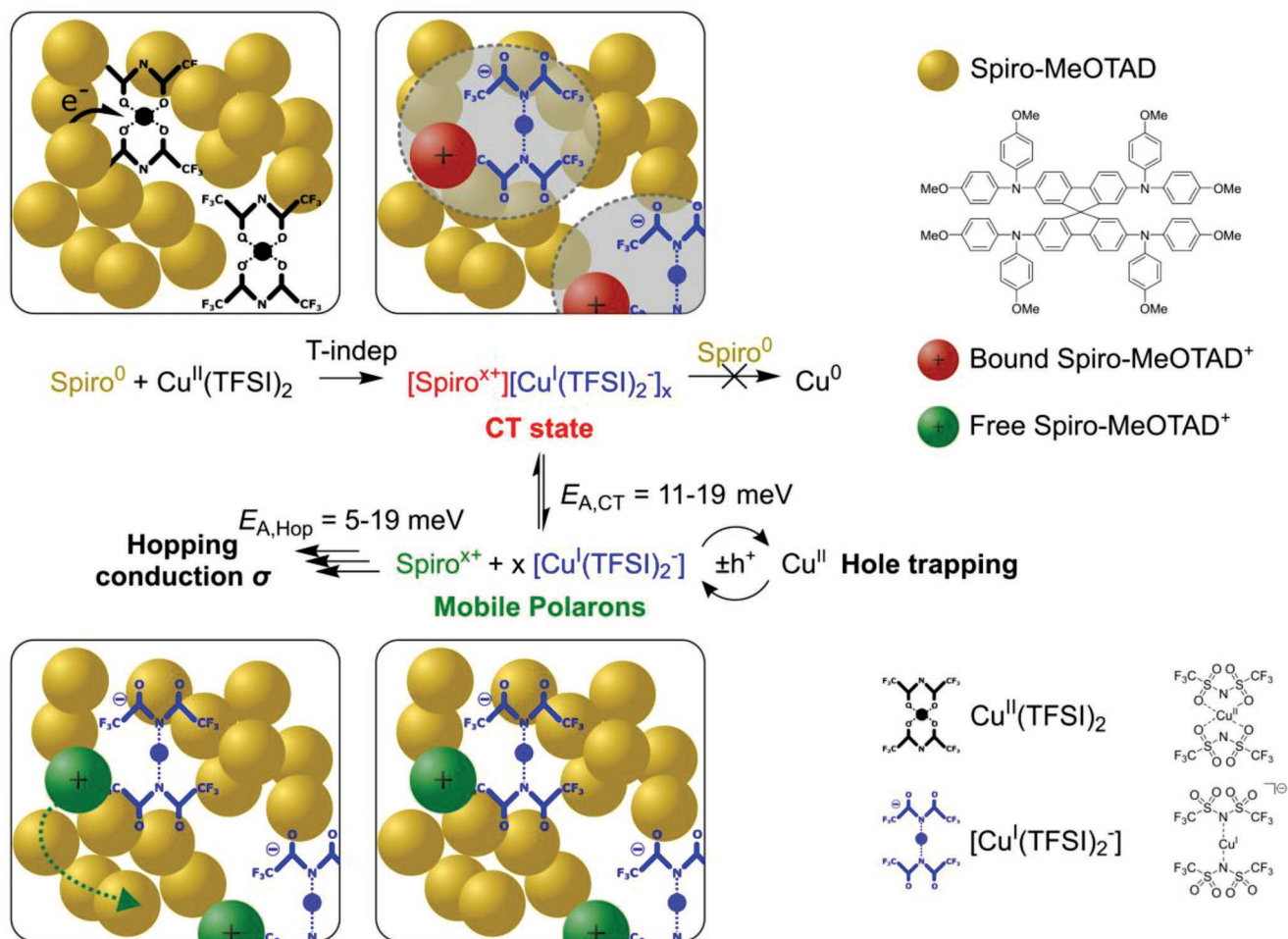
## 2.4. Hole Trapping

In our previous studies, no elemental Cu<sup>0</sup> was found in XPS studies of Cu(TFSI)<sub>2</sub> doped, co-evaporated Spiro-MeOTAD samples.<sup>[8]</sup> In turn, the Cu<sup>I</sup> state can be assumed as the final product of the doping reaction. Supplementary to the XPS studies, we tested if the doping reaction effectively stops at the Cu<sup>I</sup> oxidation state. For this, a model Cu<sup>I</sup> ion source, [Cu<sup>I</sup>(MeCN)<sub>4</sub>]<sup>+</sup>BF<sub>4</sub><sup>-</sup> having the almost identical Cu<sup>I</sup>/Cu<sup>0</sup> reduction potential compared to Cu(TFSI)<sub>2</sub> in acetonitrile solution was mixed with Spiro-MeOTAD to verify, if [Cu<sup>I</sup>(MeCN)<sub>4</sub>]<sup>+</sup> can act as a dopant (Figure S1, Supporting Information).<sup>[47]</sup> Consequently, we prepared thin films from Spiro-MeOTAD mixed with increasing mole percent of [Cu<sup>I</sup>(MeCN)<sub>4</sub>]<sup>+</sup>BF<sub>4</sub><sup>-</sup> in acetonitrile solution and conducted conductivity measurements (see Figure S17, Supporting Information, for details). Relative to pristine Spiro-MeOTAD, no increase in  $\sigma$  was found for up to 4 mol% [Cu<sup>I</sup>(MeCN)<sub>4</sub>]<sup>+</sup>BF<sub>4</sub><sup>-</sup>, the upper solubility limit of this complex in Spiro-MeOTAD. In line with XPS experiments, we conclude Cu<sup>I</sup> to be the stable oxidation state formed after reacting Cu(TFSI)<sub>2</sub> and Spiro-MeOTAD.

Penultimately, we want to clarify the role of products of the doping reaction in the macroscopic charge transport of Cu(TFSI)<sub>2</sub> doped Spiro-MeOTAD. The two possible ions arising out of doping reaction are TFSI<sup>-</sup> and Cu<sup>I</sup>. Any detrimental influence of the TFSI<sup>-</sup> anion on the charge transport was rejected for up to 10 mol% dopant concentration based on the fact that both LiTFSI(≈50 mol%)/O<sub>2</sub> or Spiro-MeOTAD(TFSI)<sub>2</sub> (17 mol% optimum) doped Spiro-MeOTAD and are known in literature to surpass the hole mobility of pristine Spiro-MeOTAD.<sup>[24,38]</sup> One may raise the question, if unbound Cu<sup>II</sup> is responsible for trapping mobile holes. Careful analysis of temperature dependent absorption helps to answer this question: i) The first step of CT state formation is temperature independent as reported in literature and verified to be valid as shown in Figure 1d for our system (see also Figures S18, S7, Supporting Information); thus, no unreacted Cu(TFSI)<sub>2</sub> should remain up to 10 mol% doping concentration ii) hypothetical Cu<sup>III</sup> as the product of hole capture by Cu<sup>II</sup> is highly unstable without suitable, stabilizing ligands.<sup>[22,48]</sup> Based on these findings, we focus on Cu<sup>I</sup> as the main trapping center for holes in this system. Using impedance spectroscopy, the effect of [Cu<sup>I</sup>(MeCN)<sub>4</sub>]<sup>+</sup>BF<sub>4</sub><sup>-</sup> on the Spiro-MeOTAD hole mobility was probed. In impedance spectroscopy experiments, a continuous decrease of the zero-field mobility  $\mu_{\text{h,0}}$  from the pristine  $(1.1 \pm 0.2) \cdot 10^{-4} \text{ cm}^2 \text{ V}^{-1} \text{ s}^{-1}$  sample to  $(4.6 \pm 0.7) \cdot 10^{-5} \text{ cm}^2 \text{ V}^{-1} \text{ s}^{-1}$  in 8 mol% [Cu<sup>I</sup>(MeCN)<sub>4</sub>]<sup>+</sup>BF<sub>4</sub><sup>-</sup>:Spiro-MeOTAD was observed (Figure 4b; Figure S19, Supporting Information). Complementary charge extraction by linearly increasing voltage CELIV measurements on Cu(TFSI)<sub>2</sub>

doped Spiro-MeOTAD revealed an identical trend of continuous decrease of the hole mobility  $\mu_{\text{h}}$  in co-evaporated samples; from  $(6.1 \pm 0.5) \cdot 10^{-7} \text{ cm}^2 \text{ V}^{-1} \text{ s}^{-1}$  in the pristine sample to  $(1.9 \pm 0.2) \cdot 10^{-7} \text{ cm}^2 \text{ V}^{-1} \text{ s}^{-1}$  at 7.5 mol% Cu(TFSI)<sub>2</sub> (Figure 4c; Figure S20, Supporting Information). As shown in our previous work, co-evaporated samples of Cu(TFSI)<sub>2</sub> and Spiro-MeOTAD are uniform and pinhole-free, excluding morphological effects on carrier mobility in this experiment.<sup>[8]</sup> Yoo et al. studied evaporated triarylamine hole conductors, chemically and energetically very similar to Spiro-MeOTAD, doped with the transition metal oxide ReO<sub>3</sub> by impedance spectroscopy and found a profound loss in hole mobility. They attributed this effect to the ionized dopants acting as coulomb traps.<sup>[49]</sup> As a consequence, Cu<sup>I</sup> is proposed to act as a hole trap by reversible oxidation to Cu<sup>II</sup>, reducing the average mobility of holes  $\mu_{\text{h}}$  in Spiro-MeOTAD. Further proof for Cu<sup>I</sup> ions acting as hole traps is the distinct [Cu<sup>I</sup>(TFSI)<sub>2</sub>]<sup>-</sup> trap state freeze-out which recovers the mobility below ≈150 K for doping concentrations >3 mol% (Figure 3b). Temperature dependent linewidth in EPR experiments verifies this hypothesis, as it suspects a lower charge carrier motion frequency above 180 K ( $E_{\text{A,trap}} \approx 16 \text{ meV}$ ) with higher  $E_{\text{A,Hop}}$ , characteristic for an increased average residence time on a “free” Cu<sup>I</sup> trap site (Figure 3e).<sup>[50]</sup>

Having identified Cu<sup>I</sup> as a potent hole trap, we verified if it is possible to disrupt the accumulation of harmful [Cu<sup>I</sup>(TFSI)<sub>2</sub>]<sup>-</sup> species in doped Spiro-MeOTAD via selective ion complexation. 2,9-Dimethyl-4,7-diphenyl-1,10-phenanthroline (Bathocuproine, abbr. BCP) proves to be a suitable ligand to achieve the targeted selectivity, as it is known to form a stable tetrahedral bis-chelating complex with Cu<sup>I</sup>.<sup>[51]</sup> Additionally, BCP stabilizes the copper(I) ion and inhibits further redox chemistry as it occurs in the hole trapping reaction.<sup>[52]</sup> We performed conductivity experiments on solution processed films, as co-evaporation does not allow sequential deposition without layered structure formation. First, Cu(TFSI)<sub>2</sub> was allowed to undergo a redox reaction with Spiro-MeOTAD in solution, then BCP was added in equimolar amounts to Cu(TFSI)<sub>2</sub> into the doped mixture solution to complex the resulting Cu<sup>I</sup> ions. Cu<sup>I</sup>(BCP)<sub>2</sub> complex formation was proven by UV/vis/NIR spectroscopy in solution and thin films (Figures S21, S22, Supporting Information). Afterward, the solution was spun-cast onto commercial interdigitated gold electrodes to determine the thin film conductivity  $\sigma$ . Following an initial strong increase, the conductivity saturates at high doping concentrations and even starts to decrease due to loss in doping efficiency and detrimental effects of by-products such as [Cu<sup>I</sup>(TFSI)<sub>2</sub>]<sup>-</sup> (Figure 4d). To our surprise,  $\sigma$  was amplified by a factor of  $0.8 \cdot 10^4$  in the presence of BCP compared to the sample without BCP at 8 mol% Cu(TFSI)<sub>2</sub>. However, we also observed a loss in solution-processed Spiro-MeOTAD film quality and disrupted morphology upon adding Cu(TFSI)<sub>2</sub> and [Cu<sup>I</sup>(MeCN)<sub>4</sub>]<sup>+</sup>BF<sub>4</sub><sup>-</sup>, similar to our previous work (Figures S23, S24, Supporting Information).<sup>[8]</sup> This effect was mitigated upon adding BCP. We argue, that morphology has minor influence on the bulk mobility, as both co-evaporated as well as solution-processed Cu(TFSI)<sub>2</sub>:Spiro-MeOTAD display almost identical thin film conductivities.<sup>[8]</sup> Therefore, we conclude that any change in  $\sigma$  originates from Cu<sup>I</sup> trap passivation. In essence, Cu<sup>I</sup> species as the doping reaction side product was identified as a potent



**Scheme 1.** Overview of the proposed individual reaction steps involving the small molecule hole-conductor Spiro-MeOTAD and *p*-dopant Cu(TFSI)<sub>2</sub>. A temperature independent and irreversible redox reaction step first yields oxidized Spiro-MeOTAD<sup>+</sup> coulombically bound to the [Cu<sup>I</sup>(TFSI)<sub>2</sub>]<sup>-</sup> counter ion (Charge transfer state). [Cu<sup>I</sup>(TFSI)<sub>2</sub>]<sup>-</sup> is generated as a side product of Cu(TFSI)<sub>2</sub> reduction. Here, Cu(II) is depicted as black, Cu(I) as blue spheres. [Cu<sup>I</sup>(TFSI)<sub>2</sub>]<sup>-</sup> traps free holes with an average trap depth of  $E_{A,\text{Trap}} = 16 \text{ meV}$ . Mobile Spiro-MeOTAD<sup>x+</sup> charge carriers are thermally released from the CT state with an activation energy  $E_{A,\text{CT}}$  in the order of 11–19 meV. Further, the free charge carrier transport responsible for the macroscopic observed conductivity in doped Spiro-MeOTAD is thermally activated with 5–19 meV.

hole trap, whose detrimental effects may be mitigated by selective complexation.

## 2.5. Absence of Elemental Cu

A final piece of the puzzle is the question concerning why no further reduction of the remaining Cu<sup>I</sup> to Cu<sup>0</sup> occurs. This is surprising, as studies have proven the capability of a Cu<sup>I</sup> iodide salt to successfully oxidize Spiro-MeOTAD with a reported copper iodide workfunction of  $\approx 5.5 \text{ eV}$ .<sup>[4,53,54]</sup> To answer this question, we refer back to cyclic voltammetry measurements on Cu(TFSI)<sub>2</sub> solutions in acetonitrile performed earlier (Figure S1, Supporting Information). Half-wave potentials of  $-0.439 \text{ V}$  versus Ag/AgNO<sub>3</sub> for Cu<sup>0</sup>/Cu<sup>I</sup> and  $+1.51 \text{ V}$  versus Ag/AgNO<sub>3</sub> of the Cu<sup>I</sup>/Cu<sup>II</sup> redox couple were recorded. These values translate to a deep lying  $EA_{\text{Cu(II)/Cu(I)}} = 6.15 \text{ eV}$ , whereas the electron affinity  $EA_{\text{Cu(I)/Cu(0)}}$  for the reduction to elemental copper is positioned at  $4.20 \text{ eV}$  in the presence of TFSI<sup>-</sup> anions and in

acetonitrile. As explained earlier, with respect to the HOMO of Spiro-MeOTAD at  $5.03 \text{ eV}$ , the high  $EA_{\text{Cu(II)/Cu(I)}}$  of Cu(TFSI)<sub>2</sub> results in an exothermic single electron transfer between Cu(TFSI)<sub>2</sub> and Spiro-MeOTAD, explaining the experimentally observed high doping efficiency. However, we noticed a low electron affinity of  $4.20 \text{ eV}$  for the reduction of [Cu<sup>I</sup>(TFSI)<sub>2</sub>]<sup>-</sup> to elemental copper, compared to  $5.5 \text{ eV}$  for CuI. Because the low EA implies an endothermic electron transfer to the HOMO of Spiro-MeOTAD, the doping reaction stops at copper(I) with the formation of [Cu<sup>I</sup>(TFSI)<sub>2</sub>]<sup>-</sup>.

We propose the  $EA_{\text{Cu(I)/Cu(0)}}$  discrepancy between copper iodide and [Cu<sup>I</sup>(TFSI)<sub>2</sub>]<sup>-</sup> lies in the stabilization of the soft Lewis acid Cu<sup>I</sup> by the adjacent ligands. Stricker et al. performed single crystal analysis on [1-ethyl-3-methylimidazolium]<sup>+</sup>[Cu<sup>I</sup>(TFSI)<sub>2</sub>]<sup>-</sup>, characterized by a d<sup>10</sup> Cu<sup>I</sup> ion coordinated linearly by the two TFSI<sup>-</sup> anions with an N<sub>TFSI,1</sub>-Cu-N<sub>TFSI,2</sub> bond angle of  $180.0^\circ$ . In this compound, TFSI<sup>-</sup> behaves as a monodentate N-donor ( $\kappa\text{N}$ ) ligand. The same cuprate(I) anion [Cu<sup>I</sup>(TFSI)<sub>2</sub>]<sup>-</sup> is very likely formed during our solvent and

oxygen free doping environment and responsible for the high stability (low  $EA_{Cu(I)/Cu(0)}$ ) via complexation and lower  $N_{TFSI-Cu}$  bond distance of  $\approx 1.9$  Å compared to I–Cu bond distance of 2.62 Å in  $\gamma$ -CuI.<sup>[55–57]</sup> To test the possibility for  $[Cu^I(TFSI)_2]^-$  formation, we mixed equimolar amounts of Spiro-MeOTAD and  $Cu(TFSI)_2$  in dichloromethane. A black, crystal-like salt was isolated by an anti-solvent approach (Figure S25, Supporting Information). A  $[Spiro-MeOTAD]^+[Cu^I(TFSI)_2]^-$  composition was determined by elemental analysis (See Supporting Information). We conclude, that energetic mismatch between  $Cu^I$  and Spiro-MeOTAD prevents reduction of  $Cu(TFSI)_2$  to elemental copper. In addition,  $[Cu^I(TFSI)_2]^-$  anions are formed in  $Cu(TFSI)_2$  doped Spiro-MeOTAD, further stabilizing the  $Cu^I$  state.

## 2.6. Doping Mechanism Overview

As a closing remark, we combined all our experimental findings to draw the complete doping mechanism between the  $p$ -dopant  $Cu(TFSI)_2$  and Spiro-MeOTAD. We propose three consecutive steps in the doping reaction: i) formation of a coulombically bound CT state  $[Spiro-MeOTAD]^{x+}[Cu^I(TFSI)_2]_{x-}$ , followed by ii) reversible, endothermic dissociation of the CT state into a free charge carrier and counterion and ultimately iii) transport of the free charge carriers with concurrent trapping involving the  $[Cu^I(TFSI)_2]^-$  anions. This concept is in line with previously published results by Tietze et al. on the doping process of zinc phthalocyanine (ZnPc) and  $N,N,N',N'$ -Tetrakis(4-methoxyphenyl)-benzidine (MeO-TPD) using the  $p$ -dopant 1,3,4,5,7,8-hexafluorotetracyanonaphthoquinodimethane  $F_6TCNNQ$ .<sup>[22]</sup> The proposed mechanism is shown in **Scheme 1**.

## 3. Conclusion

This report offers a comprehensive in-depth study of the doping process of Spiro-MeOTAD using  $Cu(II)$  salt, today one of the best hole collecting system in perovskite solar cells. The doping process itself is monitored by the observed shift of WF toward HOMO level and consequent decrease in HIB and the complex doping process is fully elucidated. Impedance and electron paramagnetic resonance spectroscopy clearly indicate low activation energies for hole release and hopping transport. Remarkably small activation barriers favor unprecedented doping efficiencies of up to 50% at 10 mol% doping using  $Cu(TFSI)_2$ . The reader is invited to recall **Scheme 1**, the central picture outlining all the important findings of this work regarding the mechanism. Prior to this study, many physical intricacies regarding  $Cu(TFSI)_2$  as a  $p$ -dopant for Spiro-MeOTAD—and in general for molecular semiconductor systems—were poorly described in literature. We could verify the temperature-independent formation of charge transfer states, in line with general agreements on doped OSCs in literature. The CT states comprised of Spiro-MeOTAD<sup>x+</sup> and  $[Cu^I(TFSI)_2]^-$  were observed to dissociate with an activation energy of  $(11.4 \pm 3.8)$  meV above  $\approx 150$  K. Due to complexation of  $Cu^I$  in the cuprate complex  $[Cu^I(TFSI)_2]^-$ , no further reduction to  $Cu^0$  can be observed. Thermal activation in the range of 5–19 meV leads to free hole hopping in the doped Spiro-MeOTAD bulk. The hole mobility was

found to be greatly influenced by reversible CT state freeze-out, causing macroscopic nonlinear temperature dependent conductivities, which cannot be explained within the framework of charge transport models.  $Cu^I$  as the dopant product was identified as a potent hole trap limiting the electrical properties. An improved understanding of this co-evaporated system provides guidelines to passivate these species using bathocuproine, resulting in vastly improved electrical conductivity. These findings complement not only earlier studies on co-evaporated  $Cu(TFSI)_2$ :Spiro-MeOTAD as a hole transport layer in solar cells, but provide crucial insight into copper salts as  $p$ -dopants for organic semiconductors.

## Supporting Information

Supporting Information is available from the Wiley Online Library or from the author.

## Acknowledgements

The authors acknowledge financial support from DFG (SPP 2196) and Bavarian State Ministry of Science and Arts (Soltech). The XPS/UPS facility (PHI 5000 VersaProbe III system) at Keylab Device Engineering in Bavarian Polymer Institute, University of Bayreuth is acknowledged. The authors thank Anna-Maria Dietel from the University of Bayreuth for conducting elemental analysis. J.G. and V.D. acknowledge support from the DFG within the Research Training School “Molecular biradicals: Structure, properties and reactivity” (GRK2112).

Open access funding enabled and organized by Projekt DEAL.

## Conflict of Interest

The authors declare no conflict of interest.

## Data Availability Statement

The data that support the findings of this study are available from the corresponding author upon reasonable request.

## Keywords

copper, doping, electron transfer, reaction mechanisms, semiconductors

Received: January 28, 2022

Revised: April 8, 2022

Published online:

- [1] S. Yue, K. Liu, R. Xu, M. Li, M. Azam, K. Ren, J. Liu, Y. Sun, Z. Wang, D. Cao, X. Yan, S. Qu, Y. Lei, Z. Wang, *Energy Environ. Sci.* **2017**, *10*, 2570.
- [2] H. J. Snaith, M. Grätzel, *Appl. Phys. Lett.* **2006**, *89*, 262114.
- [3] T. Leijtens, J. Lim, J. Teuscher, T. Park, H. J. Snaith, *Adv. Mater.* **2013**, *25*, 3227.
- [4] M. Li, Z.-K. Wang, Y.-G. Yang, Y. Hu, S.-L. Feng, J.-M. Wang, X.-Y. Gao, L.-S. Liao, *Adv. Energy Mater.* **2016**, *6*, 1601156.
- [5] C. Chen, W. Zhang, J. Cong, M. Cheng, B. Zhang, H. Chen, P. Liu, R. Li, M. Safdari, L. Kloo, L. Sun, *ACS Energy Lett.* **2017**, *2*, 497.
- [6] J. Zhang, Q. Daniel, T. Zhang, X. Wen, B. Xu, L. Sun, U. Bach, Y.-B. Cheng, *ACS Nano* **2018**, *12*, 10452.

- [7] L. Qiu, X. Zheng, J. Zhang, Y. Yang, W. Cao, Y. Dong, D. Xia, X. Zhou, R. Fan, *ACS Appl. Mater. Interfaces* **2020**, *12*, 546.
- [8] J. Mohanraj, M. Stihl, E. Simon, O. von Sicard, G. Schmidt, M. Fleischer, C. Neuber, M. Thelakkat, *ACS Appl. Energy Mater.* **2019**, *2*, 3469.
- [9] I. Salzmans, G. Heimel, M. Oehzelt, S. Winkler, N. Koch, *Acc. Chem. Res.* **2016**, *49*, 370.
- [10] M. Goel, M. Siegert, G. Krauss, J. Mohanraj, A. Hochgesang, D. C. Heinrich, M. Fried, J. Pflaum, M. Thelakkat, *Adv. Mater.* **2020**, *32*, 2003596.
- [11] T. Koopmans, *Physica* **1934**, *1*, 104.
- [12] K. Gräf, M. A. Rahim, S. Das, M. Thelakkat, *Dyes Pigments* **2013**, *99*, 1101.
- [13] S. Olthof, S. Mehraeen, S. K. Mohapatra, S. Barlow, V. Coropceanu, J. -L. Brédas, S. R. Marder, A. Kahn, *Phys. Rev. Lett.* **2012**, *109*, 176601.
- [14] A. Abate, D. R. Staff, D. J. Hollman, H. J. Snaith, A. B. Walker, *Phys. Chem. Chem. Phys.* **2014**, *16*, 1132.
- [15] M. L. Tietze, P. Pahner, K. Schmidt, K. Leo, B. Lüssem, *Adv. Funct. Mater.* **2015**, *25*, 2701.
- [16] J.-P. Yang, W.-Q. Wang, F. Bussolotti, L.-W. Cheng, Y.-Q. Li, S. Kera, J.-X. Tang, X.-H. Zeng, N. Ueno, *Appl. Phys. Lett.* **2016**, *109*, 093302.
- [17] M. L. Tietze, L. Burton, M. Riede, B. Lüssem, K. Leo, *Phys. Rev. B* **2012**, *86*, 035320.
- [18] S. Olthof, W. Tress, R. Meerheim, B. Lüssem, K. Leo, *J. Appl. Phys.* **2009**, *106*, 103711.
- [19] H. Méndez, G. Heimel, A. Opitz, K. Sauer, P. Barkowski, M. Oehzelt, J. Soeda, T. Okamoto, J. Takeya, J.-B. Arlin, J.-Y. Balandier, Y. Geerts, N. Koch, I. Salzmans, *Angew. Chem.* **2013**, *125*, 7905.
- [20] C. Lambert, G. Nöll, *J. Am. Chem. Soc.* **1999**, *121*, 8434.
- [21] S. Fantacci, F. De Angelis, M. K. Nazeeruddin, M. Grätzel, *J. Phys. Chem. C* **2011**, *115*, 23126.
- [22] M. L. Tietze, J. Benduhn, P. Pahner, B. Nell, M. Schwarze, H. Kleemann, M. Krammer, K. Zojer, K. Vandewal, K. Leo, *Nat. Commun.* **2018**, *9*, 1182.
- [23] G. Krauss, A. Hochgesang, J. Mohanraj, M. Thelakkat, *Macromol. Rapid Commun.* **2021**, *42*, 2100443.
- [24] W. Zhang, L. Wang, Y. Guo, B. Zhang, V. Leandri, B. Xu, Z. Li, J. M. Gardner, L. Sun, L. Kloo, *Chem. Commun.* **2020**, *56*, 1589.
- [25] H. Oshio, T. Watanabe, A. Ohto, T. Ito, U. Nagashima, *Angew. Chem. Int. Ed. Engl.* **1994**, *33*, 670.
- [26] A. Abate, D. J. Hollman, J. Teuscher, S. Pathak, R. Avolio, G. D'Errico, G. Vitiello, S. Fantacci, H. J. Snaith, *J. Am. Chem. Soc.* **2013**, *135*, 13538.
- [27] M. Namatame, M. Yabusaki, T. Watanabe, Y. Ogomi, S. Hayase, K. Marumoto, *Appl. Phys. Lett.* **2017**, *110*, 123904.
- [28] T. Watanabe, T. Yamanari, K. Marumoto, *Commun. Mater.* **2020**, *1*, 96.
- [29] K. Kang, S. Watanabe, K. Broch, A. Sepe, A. Brown, I. Nasrallah, M. Nikolka, Z. Fei, M. Heeney, D. Matsumoto, K. Marumoto, H. Tanaka, S. Kuroda, H. Sirringhaus, *Nat. Mater.* **2016**, *15*, 896.
- [30] A. Privitera, R. Warren, G. Londi, P. Kaienburg, J. Liu, A. Sperlich, A. E. Lauritzen, O. Thimm, A. Ardavan, D. Beljonne, M. Riede, *J. Mater. Chem. C* **2021**, *9*, 2944.
- [31] N. F. Mott, *Philos. Mag.* **1969**, *19*, 835.
- [32] B. I. Shklovskii, A. L. Efros, *Electronic Properties of Doped Semiconductors*, Springer Berlin Heidelberg, Berlin, Heidelberg **1984**.
- [33] A. V. Nenashev, J. O. Oelerich, S. D. Baranovskii, *J. Phys. Condens. Matter* **2015**, *27*, 093201.
- [34] R. Fujimoto, Y. Yamashita, S. Kumagai, J. Tsurumi, A. Hinderhofer, K. Broch, F. Schreiber, S. Watanabe, J. Takeya, *J. Mater. Chem. C* **2017**, *5*, 12023.
- [35] R. Rosenbaum, *Phys. Rev. B* **1991**, *44*, 3599.
- [36] A. L. Efros, B. I. Shklovskii, *J. Phys. C Solid State Phys.* **1975**, *8*, L49.
- [37] L. Li, N. Lu, M. Liu, *J. Appl. Phys.* **2014**, *116*, 164504.
- [38] B. Li, S. Zhang, F. Xia, Y. Huang, X. Ran, Y. Xia, Y. Chen, W. Huang, *J. Appl. Phys.* **2020**, *128*, 085501.
- [39] M. Pei, J. Guo, B. Zhang, S. Jiang, Z. Hao, X. Xu, Y. Li, *Adv. Phys. X* **2020**, *5*, 1747945.
- [40] A. Köhler, H. Bässler, *Electronic Processes in Organic Semiconductors: An Introduction*, Wiley-VCH, Weinheim **2015**.
- [41] J. A. Röhr, X. Shi, S. A. Haque, T. Kirchartz, J. Nelson, *Phys. Rev. Appl.* **2018**, *9*, 044017.
- [42] J. D. Yuen, R. Menon, N. E. Coates, E. B. Namdas, S. Cho, S. T. Hannahs, D. Moses, A. J. Heeger, *Nat. Mater.* **2009**, *8*, 572.
- [43] D. Poplavskyy, J. Nelson, *J. Appl. Phys.* **2003**, *93*, 341.
- [44] Y. Matsuo, D. Son, Y. Shimoi, K. Marumoto, *Chem. Phys. Lett.* **2014**, *607*, 29.
- [45] K. A. Peterson, A. Patterson, A. Vega-Flick, B. Liao, M. L. Chabiny, *Mater. Chem. Front.* **2020**, *4*, 3632.
- [46] M. Schwarze, C. Gaul, R. Scholz, F. Bussolotti, A. Hofacker, K. S. Schellhammer, B. Nell, B. D. Naab, Z. Bao, D. Spoltore, K. Vandewal, J. Widmer, S. Kera, N. Ueno, F. Ortman, K. Leo, *Nat. Mater.* **2019**, *18*, 242.
- [47] A. Vaskevich, I. Rubinstein, *J. Electroanal. Chem.* **2000**, *491*, 87.
- [48] A. M. Romine, N. Nebra, A. I. Kononov, E. Martin, J. Benet-Buchholz, V. V. Grushin, *Angew. Chem., Int. Ed.* **2015**, *54*, 2745.
- [49] S.-J. Yoo, J.-H. Lee, J.-M. Kim, J.-J. Kim, *Appl. Phys. Lett.* **2017**, *110*, 053303.
- [50] H. Matsui, D. Kumaki, E. Takahashi, K. Takimiya, S. Tokito, T. Hasegawa, *Phys. Rev. B* **2012**, *85*, 035308.
- [51] X. Ding, H. Xie, Y. J. Kang, *J. Nutr. Biochem.* **2011**, *22*, 301.
- [52] R. P. Patel, D. Svistunenko, M. T. Wilson, V. M. Darley-Usmar, *Biochem. J.* **1997**, *322*, 425.
- [53] P. Wang, J. Zhang, Z. Zeng, R. Chen, X. Huang, L. Wang, J. Xu, Z. Hu, Y. Zhu, *J. Mater. Chem. C* **2016**, *4*, 9003.
- [54] S. Park, H. Lee, J. Lee, Y. Lee, Y. Yi, *Org. Electron.* **2014**, *15*, 3298.
- [55] M. Stricker, B. Oelkers, C. P. Rosenau, J. Sundermeyer, *Chem. – Eur. J.* **2013**, *19*, 1042.
- [56] N. Kuganathan, J. C. Green, *Chem. Commun.* **2008**, 2432.
- [57] M. Kaiser, J. Göttlicher, T. Vitova, A. Hinz, *Chem. – Eur. J.* **2021**, *27*, 7998.